

# Plasticity and fracture of martensitic boron steel under plane stress conditions

Dirk Mohr<sup>a,b,\*</sup>, Fabien Ebnoether<sup>b,c</sup>

<sup>a</sup> Solid Mechanics Laboratory (CNRS-UMR 7649), Department of Mechanics, École Polytechnique, LMS, Room 03-1006, Palaiseau, France

<sup>b</sup> Impact and Crashworthiness Laboratory, Department of Mechanical Engineering, Massachusetts Institute of Technology, Cambridge MA, USA

<sup>c</sup> Department of Mechanical and Process Engineering, Swiss Federal Institute of Technology (ETH), Zurich, Switzerland

## ARTICLE INFO

### Article history:

Received 27 November 2008

Received in revised form 19 April 2009

Available online 22 May 2009

### Keywords:

Biaxial experiments  
Ductile fracture  
Finite element model  
Martensitic steel  
Plasticity  
Stress triaxiality

## ABSTRACT

Two series of multiaxial experiments are performed to characterize the mechanical behavior of a hot formed martensitic 22MnB5 boron steel. In the first series, flat specimens of uniform cross-section are subjected to various combinations of tensile and shear loading to characterize the elasto-plastic response. Butterfly-shaped specimens of non-uniform cross-section are used for the second series to study the onset of fracture in the martensitic steel. It is found from the analysis of the experimental results that the planar isotropic Hill'48 yield function along with an associated flow rule provides good estimates of the stress–strain response over a wide range of loading paths. The fracture experiments demonstrate that the crack initiation depends strongly on the loading state. A simple stress triaxiality dependent phenomenological fracture model is calibrated to describe the onset of fracture. Using the proposed plasticity and fracture model, numerical simulations of the fracture of tensile specimens of different notch radii are performed and compared with experiments.

© 2009 Elsevier Ltd. All rights reserved.

## 1. Introduction

There is a growing interest in automotive engineering in using martensitic steels in crash relevant structures such as the B-pillar or bumper structures. The ultimate strength of martensitic steels is typically well above 1000 MPa. Since the cold formability of martensitic steels is rather poor as compared to conventional steel grades, hot forming processes are used to make martensitic steel products. The idea is to perform the forming and the martensitic phase transformation in a single step. Starting with fully austenitic blanks, the sheets are formed and quenched in the die (e.g. Naderi, 2008). The martensite forms throughout the cooling which allows for the manufacturing of martensitic steel products of complex shape. Unlike in conventional sheet metal stamping procedures, there is almost no springback when taking a hot formed product out of the die.

Fully martensitic steels may be considered as a special member of the family of Advanced High Strength Steels (AHSS). The strength and ductility of AHSS is tailored by varying microstructural features, notably the martensite content. Dual phase steels are reinforced by adding martensite. Fully austenitic steels are initially very soft and ductile, but develop additional strength due to deformation-induced austenite-to-martensite phase transformation

(so-called TRIP effect). Most TRIP-assisted steels contain an initial volume fraction of martensite as well as retained austenite which transforms into martensite as the material deforms. Different yield surfaces have been used in the past to model AHSS steels: von Mises yield surface (e.g. Yoshida et al., 2002; Durrenberger et al., 2008), quadratic anisotropic Hill (1948) yield function (e.g. Banu et al., 2006; Padmanabhan et al., 2007; Chen and Koc, 2007), high exponent isotropic Hershey (1954) yield function (Tarigopula et al., 2008) and the non-quadratic anisotropic Barlat et al. (2003) yield function (Lee et al., 2005). Here, we perform a series of multi-axial experiments to identify a suitable yield surface for the hot formed martensitic boron steel 22MnB5.

In addition to the elastic–plastic response, the onset of fracture in martensitic steel is investigated in this work. The fracture of ductile metals is typically characterized by the nucleation and growth of voids at the microscale which coalesce to form macrocracks (McClintock, 1968). Following the work of Gurson (1977), numerous micro-mechanics based models have been developed to predict ductile fracture by describing the process of nucleation, growth and linkage of voids in metals (e.g. Tvergaard and Needleman, 1984; Voyiadjis and Kattan, 1992; Leblond et al., 1995; Pardoen and Hutchinson, 2000). This approach has also been extended to account for anisotropy due to both matrix texture and morphological anisotropy (e.g. Chien et al., 2001; Benzerga et al., 2004; Steglich et al., 2008; Danas and Ponte Castaneda, 2009). Other recent works focus on the development of micromechanics-based models for low triaxiality straining under shear-dominated states (e.g. Pardoen, 2006; Leblond and Mottet, 2008;

\* Corresponding author. Address: Solid Mechanics Laboratory (CNRS-UMR 7649), Department of Mechanics, École Polytechnique, LMS, Room 03-1006, Palaiseau, France.

E-mail address: [mohr@lms.polytechnique.fr](mailto:mohr@lms.polytechnique.fr) (D. Mohr).

Nahshon and Hutchinson, 2008; Tvergaard, 2008). The reader is referred to Lassance et al. (2007) for a comprehensive survey on the extensions of the Gurson model. As an alternative to micromechanics based approaches, phenomenological fracture models have been proposed to predict the onset of ductile fracture in uncracked bodies without modeling the evolution of the porous microstructure. Instead, it is postulated that fracture occurs when the weighted accumulative equivalent plastic strain reaches a critical value  $C$ ,

$$\int_0^{\bar{\epsilon}_f} w(\sigma) d\bar{\epsilon}_p = C, \quad (1)$$

where  $w = w(\sigma)$  represents a function of the stress state. Bao and Wierzbicki (2004) presented a comparative study on the latter class of models which included the models due to McClintock (1968), Rice and Tracey (1969), LeRoy et al. (1981) and Clift et al. (1990) and the modified Cockcroft and Latham (1968) criterion due to Oh et al. (1979). Finding an appropriate weighting function is still an active field of research. While past propositions focused mostly on the stress triaxiality as the sole parameter to describe the effect of stress state, more recent models make also use of the third stress tensor invariant to define the weighting function  $w$  (e.g. Wierzbicki and Xue, 2005). Another avenue in finding appropriate weighting functions is the transformation of stress-based fracture criteria into the space of stress triaxiality, Lode angle parameter and equivalent plastic strain (Bai, 2008).

In addition to multi-axial plasticity experiments, we make use of a newly-designed flat specimen to study the onset of fracture in martensitic steel. The specimen is subject to combinations of tensile and shear loads to characterize the crack initiation under different loading conditions. Based on the experimental data, a weighting function is proposed to describe the onset of fracture. Both the plasticity and fracture model are implemented into commercial finite element software. Notched tensile tests are performed to evaluate the proposed plasticity and fracture model at the structural level.

## 2. Material

All specimens are extracted from 1.5 mm thick hot-dipped aluminumized manganese-boron steel plates. The 22MnB5 material of the product name MBW1500 + AS has been provided by ThyssenKrupp (Germany). The  $280 \times 120$  mm large plates have been manufactured by a hot forming process under a surface pressure of about 4 MPa. Throughout quenching, the steel temperature has been reduced from 950 °C to below 100 °C in less than 15 s. Hardness tests have been performed after grinding the surface of two sheets. The average Vickers hardness obtained from measurements at more than 15 different locations on each sheet is  $VH_{10} = 467$ . The corresponding standard deviation has been less than 2% for all measurements.

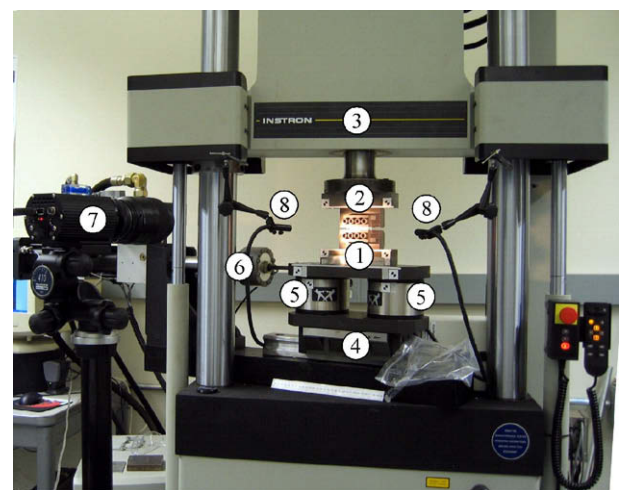
Dogbone-shaped specimens with a 32 mm long and 6 mm wide gage section have been cut from three different sheet directions (at 0°, 45° and 90° with respect to the shortest edge of the sheets). The engineering stress–strain curve for a 90° specimen is shown in Fig. 11e (blue curve). Nearly the same stress–strain curve has been recorded for specimens cut from the 0° and 90° direction while a slightly higher stress level (up to 2%) is observed for 45° specimens. The average Young's modulus is  $E = 180$  GPa. Based on the optical measurements of the width strain, we have determined an elastic Poisson's ratio of  $\nu = 0.33$ . Assuming plastic incompressibility, an average Lankford ratio of  $r = 0.9$  has been obtained. This ratio appeared to be independent of the specimen orientation. Thus, the martensitic sheet material is considered as planar isotropic throughout this study.

## 3. Experimental procedures

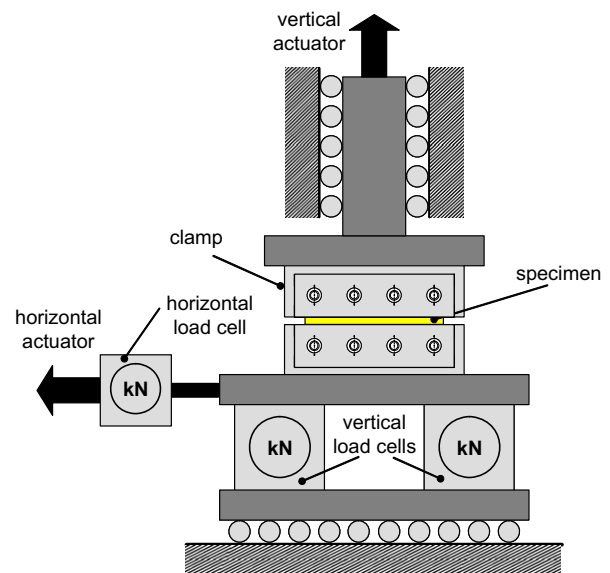
Two newly-developed biaxial testing techniques are employed in this study. The first is used to characterize the elasto-plastic behavior of the martensitic steel, while the second is used to investigate the onset of fracture. The backbone of both experimental techniques is a custom-made dual actuator system (Fig. 1a). This system is used to apply tangential and normal loads to the boundaries of a flat specimen. As illustrated in Fig. 1b, the lower specimen clamp is mounted onto a low friction sliding table. A load cell positioned between the horizontal actuator and the lower specimen clamp measures the tangential force. The normal force is applied through the vertical actuator in the upper cross-head. Two additional load cells have been integrated into the lower sliding table to measure the total vertical force.

### 3.1. Biaxial plasticity experiments

Fig. 2a shows the shape and dimensions of the plasticity specimen. The reader is referred to Mohr and Oswald (2008) for details



(a)



(b)

Fig. 1. (a) Dual actuator loading system: 1 – lower specimen grip, 2 – upper grip, 3 – upper cross-head, 4 – sliding table, 5 – vertical load cells, 6 – horizontal load cell and actuator, and 7 – digital camera. (b) Schematic of the mechanical system.

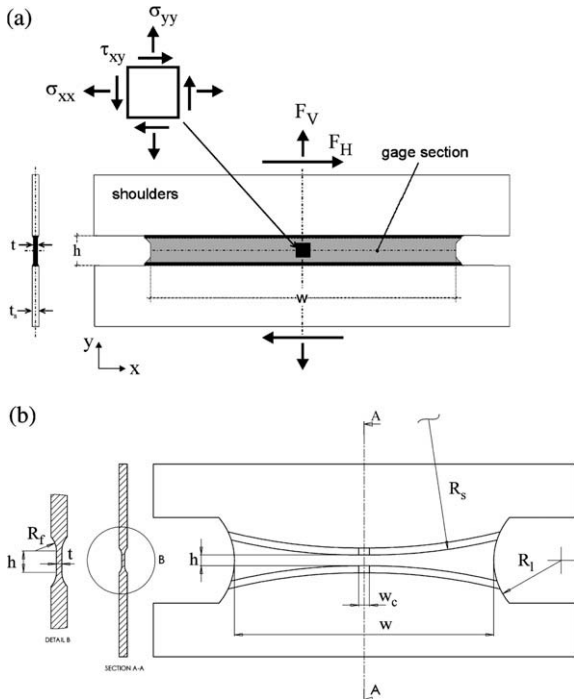


**Fig. 2.** Specimen geometries: (a) plasticity specimen of width  $w = 50$  mm, shoulder thickness  $t_s = 1.5$  mm, gage section thickness  $t = 0.45$  mm, (b) fracture specimen of dimensions  $R_s = 100$  mm,  $R_f = 12.5$  mm,  $R_1 = 2$  mm,  $w_c = 2$  mm,  $t = 0.45$  mm,  $h = 2$  mm and  $w = 48$  mm.

on the specimen development. The specimen features a 5 mm high and 50 mm wide gage section. The thickness of the gage section has been symmetrically reduced to about 0.5 mm using a CNC milling center. Both the choice of coated cutters and the cooling system required special attention as the martensite is easily destroyed by the heat developed during machining. The displacements are measured directly on the specimen surface using a digital image correlation system (VIC2D, Correlated Solutions Inc, SC). More than 200 photographs are taken throughout each monotonic experiment. The data are acquired using the software packages FastTrack DAX (Instron, Canton, MA) and VicSnap (Correlated Solution, SC).

The experimental technique allows for the testing of the sheet material for different combinations of normal and shear loading. As illustrated in Fig. 2a, we define the so-called *biaxial loading angle*  $\beta$ ,  $0^\circ \leq \beta \leq 90^\circ$ , to quantify the ratio of normal to shear loads,

$$\tan \beta := \frac{F_V}{F_H}. \quad (2)$$

The limiting cases of  $\beta = 0^\circ$  and  $\beta = 90^\circ$  correspond to pure shear and transverse plane strain tension, respectively.

In our discussion, we refer to the horizontal and vertical axis as  $x$ - and  $y$ -direction, respectively. As demonstrated by Mohr and Oswald (2008), the specimen is designed such that the engineering stress along the  $y$ -direction,  $\Sigma_y$ , may be approximated by

$$\Sigma_y \cong \frac{F_V}{A_0} \quad (3)$$

with the initial cross-sectional area  $A_0 = wt$ . Eq. (3) implies that the variations of the stress  $\Sigma_y$  are negligible along the  $x$ -direction. Similarly, due to the large width-to-height ratio, we may assume that the shear stress variations along the  $x$ -direction are small. Hence, the engineering shear stress  $\Sigma_{xy}$  associated with the horizontal force measurement  $F_H$  reads

$$\Sigma_{xy} \cong \frac{F_H}{A_0}. \quad (4)$$

The corresponding engineering normal strain  $E_y$  and engineering shear strain  $E_{xy}$  are determined from DIC. Note that the strain along the  $x$ -direction is approximately zero,  $E_x \cong 0$ . In other words, the state of stress in the specimen gage section is plane stress, while the state of deformation in this specimen is transverse plane strain.

### 3.2. Biaxial fracture experiments

Even though the plasticity specimen features highly uniform stress and strain fields throughout the gage section, these fields are slightly perturbed in the vicinity of the free gage section boundaries. Irrespective of the biaxial loading angle, the stress state is always uniaxial at the free boundaries of a plane stress specimen. Therefore, cracks frequently initiate under uniaxial conditions near the specimen boundaries although the uniform stress state throughout the gage section is very different (e.g. pure shear). In order to overcome this problem, Mohr and Henn (2004, 2007) proposed a butterfly shaped specimen that focuses the deformation at the specimen center, thereby minimizing the risk of crack initiation near the specimen boundaries. Different derivatives of the butterfly specimen have been proposed in the recent literature (e.g. Wierzbicki et al., 2005). The geometry of the present butterfly specimen shown in Fig. 3b has been chosen based on the results of Mohr and Dunand (2008). It features a small flat central area where the strain and stress fields are expected to be uniform prior to necking.

By varying the biaxial loading angle, the material may be tested under different stress triaxialities. Here, we define the stress triaxiality  $\eta$  through the negative ratio of the hydrostatic pressure  $p = tr(\sigma)$  and the von Mises equivalent stress  $\bar{\sigma}_{Mises}$ ,

$$\eta = -\frac{p}{\bar{\sigma}_{Mises}}. \quad (5)$$

The stress triaxiality is zero for pure shear loading while it reaches its maximum of  $\eta = 2/3$  under plane stress conditions for equibiaxial loading. The stress triaxiality for transverse plane strain tension ( $\beta = 90^\circ$ ) is  $1/\sqrt{3} \cong 0.57$  in the case of a Levy-von Mises material. All experiments are performed under force control. The only exceptions are the pure shear tests where the horizontal position was controlled while keeping  $F_V = 0$ , and the test at  $\beta = 90^\circ$  which has been performed under full position control.

The strains in the gage section are determined using digital image correlation. The photographs are taken typically taken at a fre-

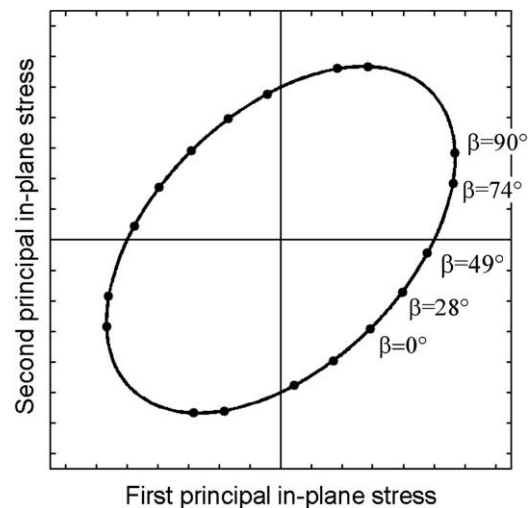


**Fig. 3.** Planar isotropic Hill'48 yield surface for  $\bar{r} = 0.9$ . The solid dots highlight the points on the yield surface that describe the stress states covered by the biaxial testing program.

quency of 1 Hz using a digital monochrome camera with a  $1300 \times 1030$  pixel sensor field. Using a set of macro-lenses (Nikon Nikkor Micro 105 mm), a field of view of about  $13 \times 10$  mm is recorded (which corresponds to a pixel size of about  $10 \mu\text{m}$ ). The typical size of the black spray paint speckles was about 10 pixels. Throughout our DIC analysis, quintic B-spline interpolation of the gray values is used to achieve sub-pixel accuracy. The displacement field of all pixels in the area of interest is calculated based on the assumption of an affine transformation of the  $29 \times 29$  pixel neighborhood of each pixel. The Lagrangian strains<sup>1</sup> are calculated based on the approximation of the displacement gradient within a local neighborhood of 15 pixels. Thus, for a displacement measurement accuracy of  $\pm 0.1$  pixels, the estimated accuracy of the calculated strains is about  $\pm 0.1/15 = 0.007$ .

#### 4. Plasticity

Biaxial plasticity tests are carried out for five different biaxial loading angles:  $\beta = 0^\circ, 28^\circ, 49^\circ, 74^\circ$  and  $90^\circ$ . The intersection points of the corresponding loading paths with the plane stress yield surface in the principal stress plane are shown in Fig. 3 (black solid dots). Two stress–strain curves are obtained from each biaxial experiment. The normal stress versus normal strain curves are depicted in Fig. 4a (dashed black lines), while Fig. 4b shows the corresponding shear stress versus shear strain curves. All curves are in hierarchical order, i.e. they are in order with respect to the biaxial loading angle and do not intersect each other. Engineering shear strains of up to 0.28 could be achieved before cracks became visible at the specimen boundaries. For transverse plane strain tension ( $\beta = 90^\circ$ ), the maximum normal strain was 0.035 before necking occurred.

We make use of the planar isotropic version of the Hill'48 yield surface to model the material's plastic behavior. The yield condition reads

$$f(\sigma, k) = \bar{\sigma}_{\text{Hill}} - k = 0. \quad (6)$$

where  $\bar{\sigma}_{\text{Hill}}$  denotes the equivalent Hill stress

$$\bar{\sigma}_{\text{Hill}} = \sqrt{\sigma_x^2 + \sigma_y^2 - 2\left(\frac{r}{1+r}\right)\sigma_x\sigma_y + 2\left(\frac{1+2r}{1+r}\right)\tau^2} \quad (7)$$

with  $r = 0.9$ . In the framework of isotropic hardening, the deformation resistance  $k$  is defined as a function of the work-conjugate equivalent plastic strain,  $k = k(\bar{\epsilon}_p)$ . The piece-wise linear function  $k(\bar{\epsilon}_p)$  has been determined from the pure shear experiment. An associated flow rule is employed to describe the evolution of the plastic strain tensor.

The solid curves in Fig. 4a and b show the model estimates of the engineering stress–strain curves for combined loading. All curves except that labeled  $\beta = 0^\circ$  in Fig. 4b may be interpreted as model predictions. The comparison with the dashed experimental curves demonstrates that the planar isotropic Hill model with associated flow and isotropic hardening provides an accurate description of the material's response for monotonic multi-axial loading conditions. As illustrated in Fig. 3, the stress state in a biaxial experiment at  $\beta = 49^\circ$  is very close to uniaxial tension. The corresponding curves in Fig. 4 demonstrate that the model provides excellent predictions of the stress–strain curves for this loading angle. However, the model overestimates the stress level in uniaxial tensile tests on dogbone shaped specimens. Fig. 5 compares the

<sup>1</sup> Even though the plasticity model will be formulated in terms of Cauchy stresses and logarithmic strains, some DIC results are presented in terms of Lagrangian strains. The VIC 2D DIC software provides Lagrangian strains. These can be converted into logarithmic strains, but this calculation has been omitted unless the DIC measurements are compared with the simulation results.

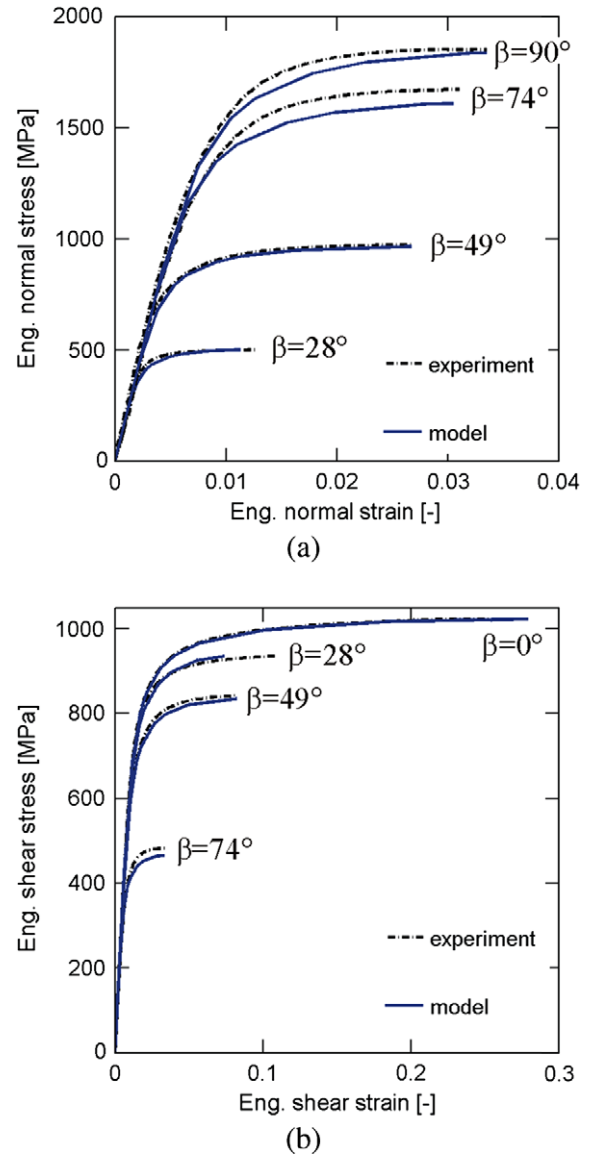


Fig. 4. Stress–strain behavior of the martensitic steel under biaxial loading. The experimental data are depicted by dashed lines while the solid lines represent the corresponding predictions of selected plasticity models.

stress–strain curve  $k = k(\bar{\epsilon}_p)$  determined from shear testing (solid curve) with that obtained from uniaxial tensile testing (dashed curve). Recall that the shear curve has been used to calibrate the plasticity model for the biaxial simulations. Because of the good agreement between the experiments and the simulations, it therefore also represents the equivalent stress–strain curve for  $\beta = 49^\circ$ . This difference of about 10% in the stress level between the curves shown in Fig. 5 is attributed to microstructural changes induced during the machining of the specimens. A material property gradient along the thickness direction of this 1.5 mm thick sheet material may also be responsible for this difference.

#### 5. Fracture

##### 5.1. Experimental results

The fracture specimens are tested at the biaxial loading angles  $\beta = 0^\circ, 52^\circ, 63^\circ, 75^\circ$  and  $90^\circ$ . Throughout each experiment, we took a sequence of at least 200 photographs prior to fracture.

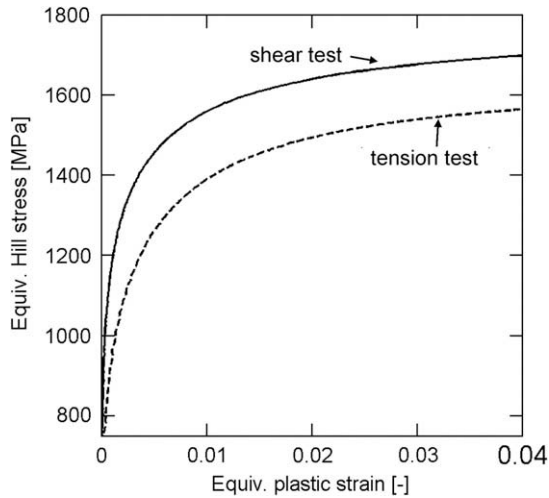


Fig. 5. Comparison of the stress–strain curves obtained from the shear testing (solid curve) and the tensile testing of dogbone specimens (dashed curve).

After calculating the displacement of each pixel within the area of interest based on the DIC analysis, the Lagrangian strains have been computed from the least square fit of the deformation gradient over a neighborhood of 15 pixels. Representative contour plots of the corresponding maximum principal strain fields are shown in Fig. 6. All plots have been evaluated using the last picture recorded before cracks became visible at the specimen surfaces. The initial DIC measurement window size (dashed rectangular frames in Fig. 6) is about  $10 \times 3.5$  mm. Irrespective of the loading angle, a localization band becomes visible that precedes the initiation of fracture. All material points within the inner contour lines in Fig. 6 are strained to at least 80% of the maximum strain value determined from DIC analysis. The zone defined by the inner contour line is about 0.1–0.2 mm wide in the case of transverse plane strain tension (Fig. 6d). Depending on the biaxial loading angle, the size of this zone increases up to 0.5 mm (Fig. 6b).

It is noted that the DIC strain calculations imply the filtering of the displacement field. At the same time, the calculated displacement field contains artificial noise which may also cause local variations in the strain field. Therefore, we also show the cross-sectional cuts of the corresponding vertical and horizontal displacement field at the location of the highest principal strain (Figs. 7 and 8). Fig. 7a shows the vertical displacement field at various instance in a specimen loaded at  $\beta = 90^\circ$ . At an early stage of the experiment, the displacement field is approximately linear along the y-direction (green line), while the kink in the subsequent vertical displacement profiles indicates the localization of deformation. Each dot of the curves shown in Fig. 7a depicts the displacement of a pixel within the DIC measurement window. Observe that the displacement field remains linear within a neighborhood of about 15 pixels (about  $150 \mu\text{m}$ ). Fig. 7b shows the corresponding variation of the horizontal displacement during a pure shear test ( $\beta = 0^\circ$ ). As for the tensile experiment, the displacement field is more or less linear within a region of  $150 \mu\text{m}$ . Parts of the blue and black curve lie on top of each other indicating that the stresses remained constant while the deformation localized. Similar conclusions may be drawn from the displacement profiles for biaxial loading (see Fig. 8).

### 5.2. Determination of the fracture locus

The specimens have been designed such that the stress triaxiality is uniform within the gage section (Mohr and Dunand, 2008).

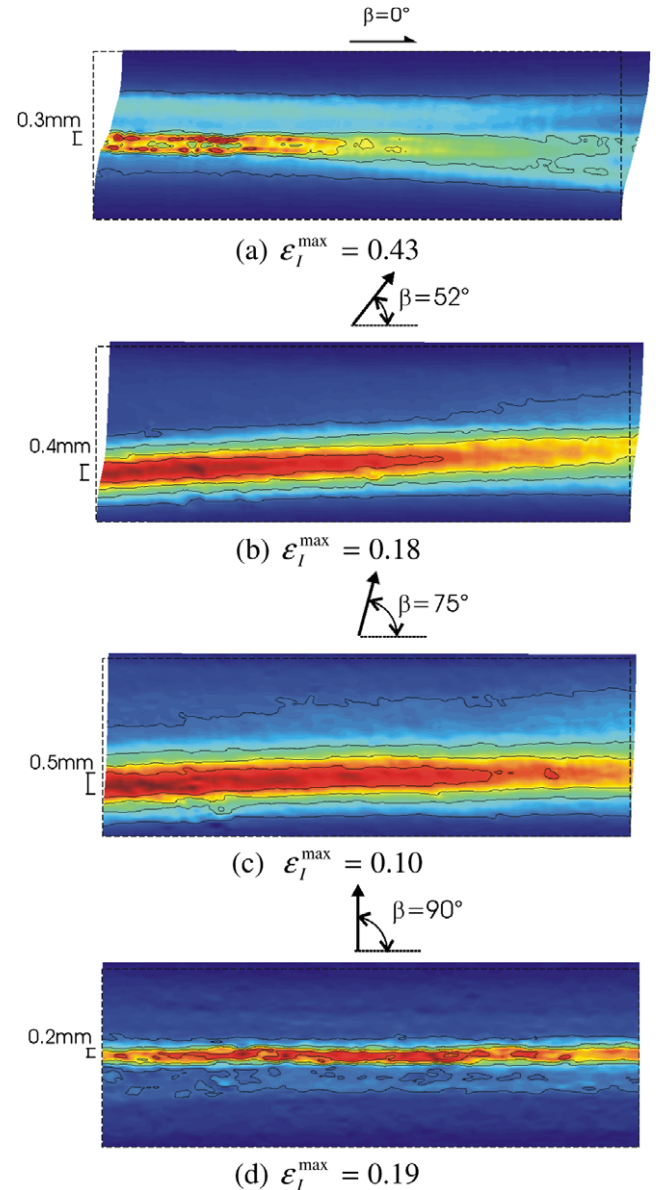
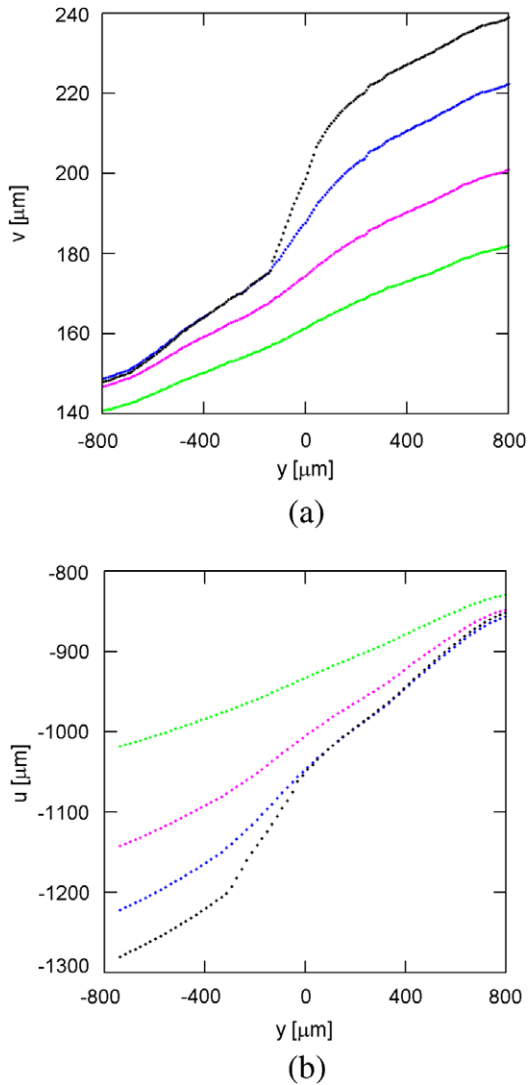


Fig. 6. Principal strain fields determined from DIC analysis within a central area of about  $10 \times 3.5$  mm of the gage section. The dashed lines indicate the initial size of this area. The contour lines are drawn for 20%, 40%, 60% and 80% of the maximum principal Lagrangian strain value given below each plot.

Therefore, it is assumed that fracture initiates at the point within the gage section where the equivalent plastic strain is the highest. The DIC measurements provide only the total strains. Thus, in close analogy with the equivalent plastic strain definition for linear loading paths, we assume that fracture occurs at the location where the deformation measure

$$\varepsilon^* = \sqrt{\varepsilon_1^2 + \varepsilon_2^2} \quad (8)$$

reaches its maximum. In (8),  $\varepsilon_1$  and  $\varepsilon_2$  denote the principal Lagrangian strains. Evaluation of the experimental data revealed that this location is typically close to the location of the highest maximum principal strain. Assuming radial loading and rigid plastic material behavior, we estimated the stress triaxiality based on the ratio  $\varepsilon_1/\varepsilon_2$  (see Mohr and Henn, 2007 for details). Fig 9a–e shows the corresponding plots of  $\varepsilon^*$  as a function the stress triaxiality estimates. Each dot in Fig. 9 represents the strain state at a pixel within the DIC



**Fig. 7.** Cuts through the section of maximum principal strain: (a) vertical displacement profile for transverse plane strain tension ( $\beta = 90^\circ$ ), and (b) horizontal displacement profile for pure shear ( $\beta = 0^\circ$ ).

measurement areas depicted in Fig. 6. The overall shape of the point clouds indicates that each specimen features a small range of stress triaxialities at which the largest strains are reached.

In order to calculate the equivalent plastic strain and stress triaxiality from each experiment, we performed the following procedure:

1. Identification of the location within the gage section where the highest value of  $\varepsilon^*$  is observed prior to fracture.
2. Calculation of the time history of the minor and major principal strains at this location. Both strains are defined through the spatial average within a window of  $15 \times 15$  pixels.
3. Numerical solution of the constitutive equations (planar isotropic Hill'48 model) to determine the corresponding evolution of the stress triaxiality and equivalent plastic strain.

The dotted black lines in Fig. 10 show the evolution of the equivalent plastic strain  $\bar{\varepsilon}^p$  as a function of the average stress triaxiality (moving average),

$$\langle \eta \rangle = \frac{1}{\bar{\varepsilon}_p} \int_0^{\bar{\varepsilon}_p} \eta d\bar{\varepsilon}_p. \quad (9)$$

The curves are only shown for the experiments that yielded the highest ductility for the same biaxial loading angle. The end point of each loading trajectory is highlighted by a large blue dot. In addition to the results obtained from the present series of experiments, we added one data point that has been obtained from the punch testing of a circular disc (50 mm punch diameter). The numerical values of all end points are given in Table 1.

The results indicate that the “ductility” (here: max. equivalent plastic strain) of the martensitic steel is the lowest at a stress triaxiality of 0.53 ( $\beta = 75^\circ$ ). The ductility increases from its minimum value of 0.083–0.39 when increasing the stress triaxiality up to its plane stress maximum of  $2/3$ . The ductility also increases when reducing the average stress triaxiality from 0.47 to 0.39. As observed by Bao (2003) in aluminum, the equivalent plastic strain versus stress triaxiality curve appears to feature a second minimum between 0 and 0.39. For modeling purposes, we assume a piecewise linear function  $g(\eta)$  to describe the failure envelope  $\bar{\varepsilon}_p^{\max} = g(\eta)$ . Subsequently, this function is used to determine the weighting function  $w(\sigma)$  of the phenomenological fracture model (Eq. (1)). Formally, we define the damage parameter

$$D = \int_0^{\bar{\varepsilon}_f} w(\sigma) d\bar{\varepsilon}_p = \int_0^{\bar{\varepsilon}_f} \frac{d\bar{\varepsilon}_p}{g(\eta)} \quad (10)$$

such that the model predicts fracture when  $D = 1$ . According to (9), damage is accumulated throughout plastic loading. Furthermore, the damage is irreversible since  $g(\eta) \geq 0$  for any stress triaxiality. However, the effect of damage on the elasto-plastic material properties is not taken into account by the present model. In other words, there is no coupling between the fracture and plasticity. In a first approximation, the stress triaxiality may be considered as constant throughout the loading of a butterfly specimen. For constant stress triaxialities, Eq. (10) yields

$$g(\eta) = \bar{\varepsilon}_f \quad \text{at} \quad D = 1. \quad (11)$$

Hence the support points of the piece-wise linear function  $g(\eta)$  are  $g(\langle \eta \rangle^{(i)}) = \bar{\varepsilon}_f^{(i)}$  where  $\bar{\varepsilon}_f^{(i)}$  denotes the equivalent plastic strain to fracture in the experiment  $i$ .

### 5.3. Application of the fracture locus

There are several aspects which need to be noted regarding the application of the determined fracture locus. The loading history to fracture has been determined at the specimen surface. Whenever necking is present prior to fracture, the stress triaxiality and equivalent plastic strain are expected to be higher near the specimen mid-plane than at the specimen surface. In other words, fracture may have started from the inside of the specimen. Therefore, the present fracture locus may be interpreted as a lower bound, i.e. the material is always intact for  $D < 1$ , while  $D > 1$  is a necessary but not sufficient condition for the onset of fracture. There is also an experimental argument confirming this lower bound property of the determined fracture envelope. If the static force–displacement curve for an experiment features a force maximum prior to fracture, the hydraulic control system will request an acceleration of the piston at the force maximum in an attempt to increase the force level further. Theoretically, the force can only increase with the help of the inertia of the specimen. In practice, the strains within the specimen will increase rapidly until specimen fracture. In the present experiments, the strains have been recorded at a frequency of about 1 Hz. Thus, the surface strains determined from the last picture before fracture are smaller than the surface strains at fracture.

The application of the fracture locus in engineering practice requires finite element simulations that can predict the strains and stresses after the onset of necking. The prediction accuracy relies heavily on the quality of the plasticity model and the spatial dis-

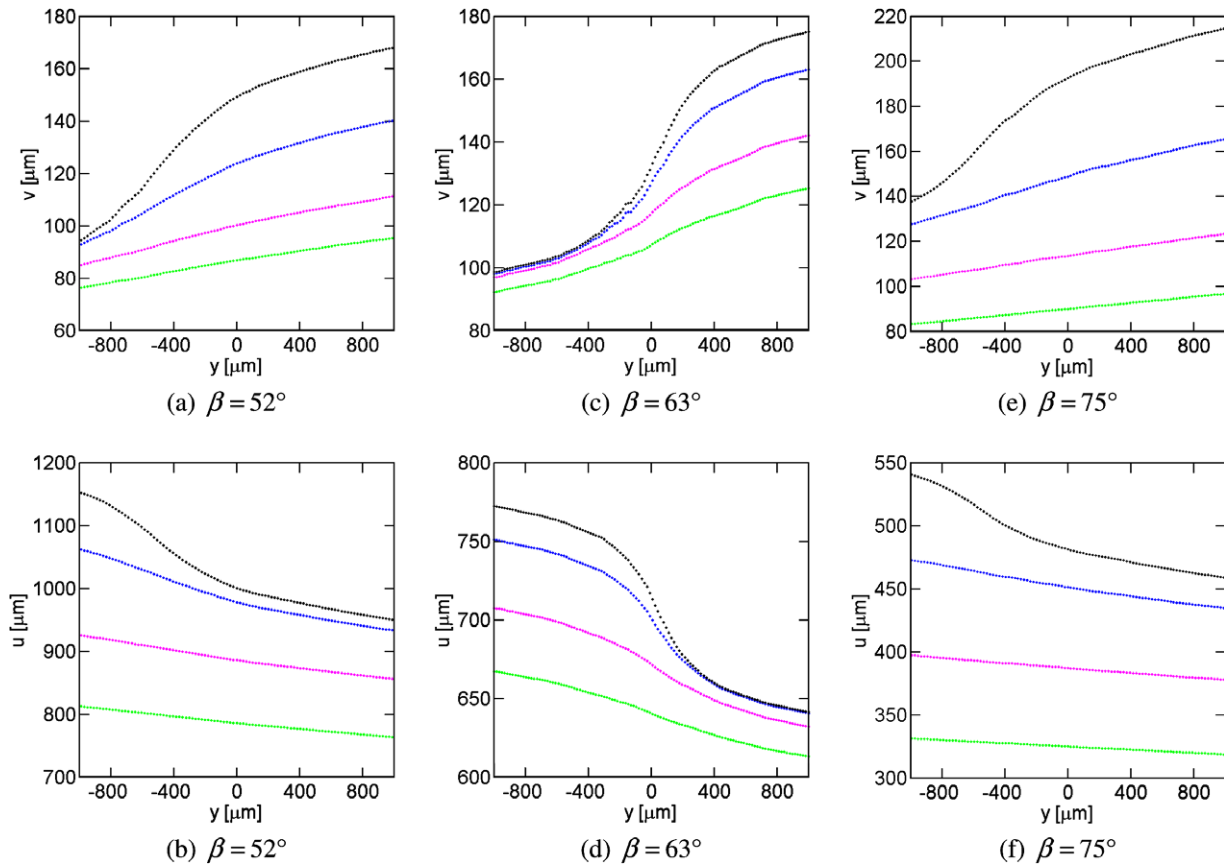


Fig. 8. Cut through the displacements field at the location of the highest maximum principal strain.

cretization. In particular, the extrapolation of the true stress–strain curve obtained from uniaxial tensile testing is important. Shell element models are usually not able to model through-the-thickness necking adequately. Solid element models are able to estimate the stress and strain histories during necking. It is important to use sufficiently fine meshes (converged solution with respect to the mesh size). In some structural problems, the force–displacement response is not very sensitive with respect to the mesh density, but the local strain and stress fields within a neck are usually very mesh size sensitive. However, since the boundary value problem is well posed throughout necking (as long as  $dk/d\bar{\epsilon}_p > 0$ ), the numerical solutions will converge to the exact unique solution for sufficiently fine meshes.

## 6. Validation and discussion

In an attempt to validate the proposed fracture model, we perform numerical simulations of notched tensile tests. The simulation results are compared with experiments and discussed in detail. Furthermore, an enhanced fracture model is proposed to improve the prediction accuracy.

### 6.1. Notched tensile tests

Specimens with three different notch radii are extracted from the hot-formed martensitic steel plates using a water-jet. All specimens are 20 mm wide in the gripping area and featured a  $b = 10$  mm wide notched gage section. The different notch radii are  $R = 20$  mm, 10 mm and 6.67 mm. All experi-

ments are performed under displacement control at a cross-head speed of less than 10 mm/min. Throughout the experiments, we use an optical extensometer (DIC) to determine the relative displacement  $\Delta u$  of two points within the bottom and top specimen shoulder (initial spacing of 34 mm). The measured force–displacement curves are shown by black solid lines in Fig 13a–c. Each curve exhibits a force peak before fracture occurs. The displacement to fracture decreases from 1.13 mm to 0.8 mm as the notch radius decreases from 20 mm to 6.67 mm. Two experiments have been performed for each notch radius and confirmed excellent repeatability as far as the force–displacement curve is concerned.

### 6.2. Finite element modeling

The finite element program Abaqus (2007) is used to perform the numerical simulations of the notched tensile experiments. The specimen geometries have been discretized with 8-node reduced-integration brick elements. The planar isotropic Hill'48 yield function is used in conjunction with an associated flow rule and an isotropic hardening law. The extrapolation of the stress–strain curve  $k = k(\bar{\epsilon}^p)$  for plastic strains larger than 0.04 (onset of necking) is determined from the numerical simulation of a uniaxial tensile test. This approach has been adopted by various authors (e.g. Norris et al., 1978; Pardoen and Delannay, 1998; Bao, 2003). The required minimum mesh density is subsequently determined from simulations of the tensile specimen with the smallest notch, before predicting fracture of all specimens using the empirical fracture model.

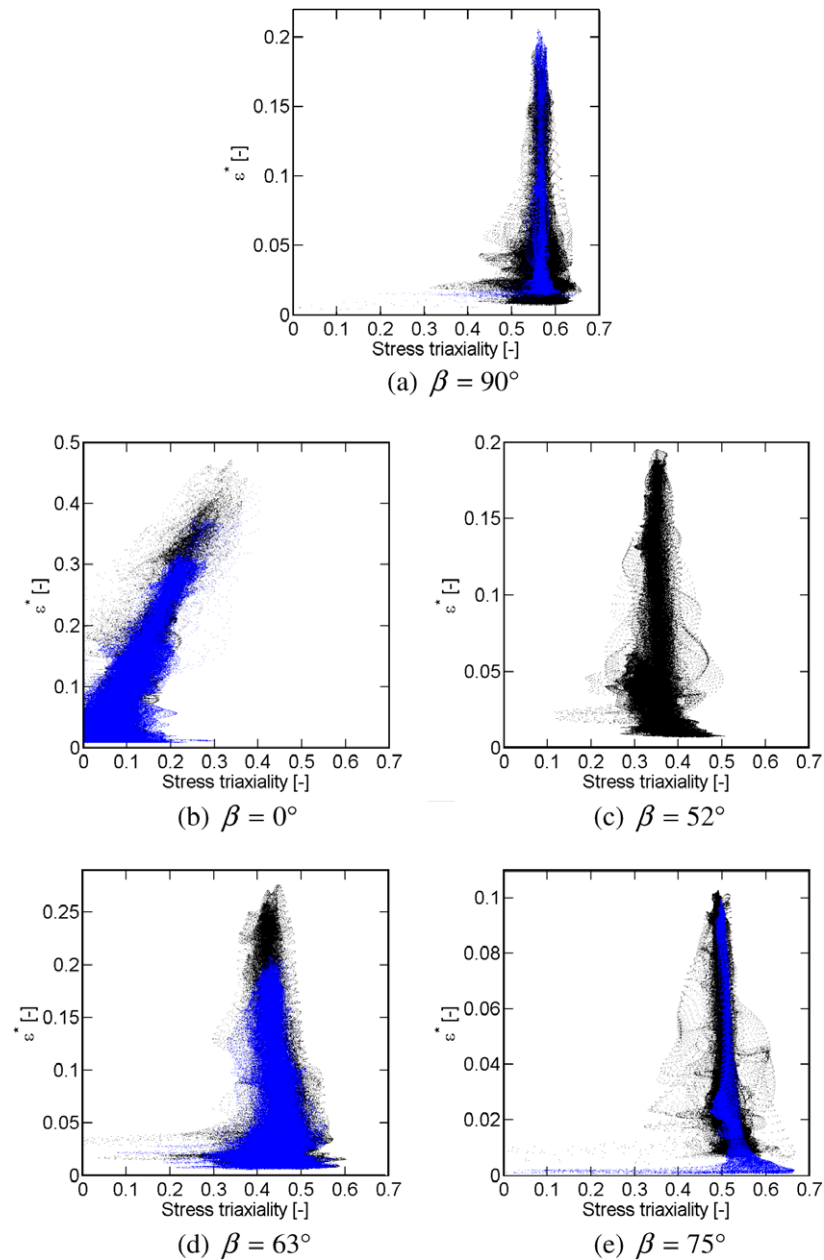


**Fig. 9.** Visualization of the loading state prior to failure based on DIC measurements. The abscissa corresponds to an estimate of the stress triaxiality based on the stress ratio  $\varepsilon_{II}/\varepsilon_I$ ; the ordinate  $\varepsilon^* = \sqrt{\varepsilon_I^2 + \varepsilon_{II}^2}$  may be interpreted as equivalent strain magnitude.

### 6.2.1. Extrapolation of the true stress–strain curve

As described in Section 2, uniaxial tensile tests have been performed on 6 mm wide dogbone shaped specimens. We determined the engineering stress versus engineering strain curve (Fig. 11e) using a virtual extensometer length of 6.5 mm for an experiment where the local neck formed close to the center of the DIC window. A series of pictures of the deformed specimen is shown in Fig. 11a–c. The corresponding data points on the engineering stress–strain curves have been highlighted in Fig. 11e. Fracture is observed at an engineering strain of 0.2. The failed specimen is shown in Fig. 11d.

Several mesh densities are considered. A coarse finite element mesh of an eighth of the tensile specimen is shown in Fig. 11f. It features four elements along the thickness-direction. The cross-sectional area at the specimen center is reduced by 1% in the ini-

tial configuration. This geometric imperfection is introduced to trigger the neck development at the center of the numerical specimen. Subsequently, the engineering stress–strain curve is determined from the numerical simulation using the same gage length as in the DIC analysis. The use of an eighth model may lead to higher dissipation than a half or full model. However, as shown by Besson et al. (2003), the effect of this constraint may be neglected prior to slant localization (possible final stage of ductile fracture).

We determined the true stress versus logarithmic plastic strain curve from the experiment until the onset of necking (corresponds to a plastic strain of 0.04). As suggested by Byun et al. (2004), a constant extrapolation modulus  $H$  is assumed for larger strains. The lower dashed curve in Fig. 11e depicts the model prediction for  $H = 0$ . The upper dashed curve is ob-

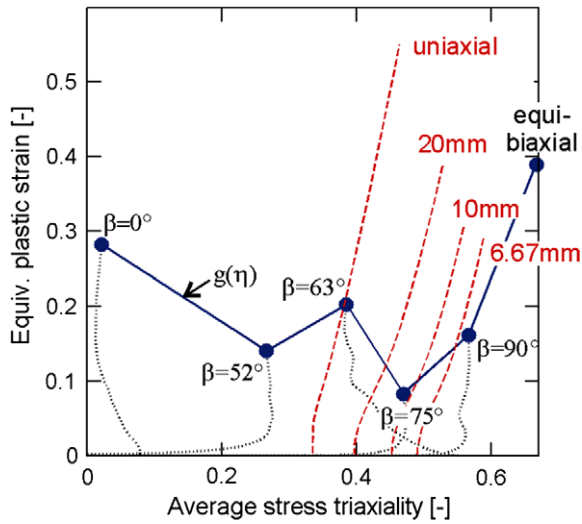


**Fig. 10.** Determination of a piecewise-linear fracture envelope (blue line) after calculating the evolution of the equivalent plastic strain and the average stress triaxiality from the DIC measurements from different biaxial fracture tests (dotted lines). The data point for equi-biaxial loading is obtained from a punch test. The red dashed curves are obtained from finite element simulations of the uniaxial and notched tensile tests; all blue curves have been determined based on surface strain measurements, while the dashed red curves correspond to the simulation results at the specimen mid-plane (center). (For interpretation of the references to color in this figure legend, the reader is referred to the web version of this paper.)

**Table 1**  
Data points of the piece-wise linear fracture envelope  $g(\eta)$ .

$\eta$	0.022	0.267	0.385	0.470	0.567	0.667
$g$	0.282	0.140	0.203	0.083	0.162	0.390

tained when the hardening modulus is determined from the linear extrapolation of the measured true stress versus plastic strain curve ( $H = 3000$  MPa). The best agreement between the model prediction and the measured engineering stress-strain curve is found for  $H = 532$  MPa (solid black curve in Fig. 11e, Table 2). This simulation has been repeated for a finer mesh to rule out the mesh dependence of the previous engineering stress-strain curve estimate.

6.2.2. Mesh size

Here, we focus on the effect of the mesh size on the local stress and strain fields in the simulation of notched tensile tests. Fig. 12c–f shows details of four different meshes of the specimen with a 6.67 mm notch. The edge length (in the specimen width direction) of the smallest elements near the specimen center is 0.5, 0.25, 0.125 and 0.055 mm for the coarse, medium, fine and very fine meshes, respectively. The corresponding number of elements along the thickness-directions is 2, 4, 6 and 8. The simulations are performed up to the experimentally-measured displacement to fracture of  $\Delta u_f = 0.8$  mm. Fig. 12a shows the predicted stress-strain curves which appear to be almost independent of the mesh sizes (all four curves lie on top of each other). The evolution of the equivalent plastic strain at the integration point of the element closest to the specimen center is shown in Fig. 12b; it is depicted as a function of the applied displacement  $\Delta u$ . The final plastic strain predicted using the coarse mesh is 0.19, while the corresponding estimates based on much finer meshes is close to 0.3. The comparison of these curves indicates that the predictions are close for the fine and very fine meshes. In other words, the fine mesh seems to provide an adequate description of the stress and strain fields near

the specimen center. Consequently, all meshes used in the subsequent simulations have at least 6 elements through-the-thickness and 20 elements across the least width of the eighth model of the specimen.

6.3. Fracture prediction

The proposed fracture model has been implemented into the finite element software through the user material subroutine. Fig. 13 shows the predicted force-displacement curves (dashed lines) for the three notch radii as solid lines next to the experimental curves (solid lines). The overall agreement is very good. The blue dashed curves of convex shape show the evolution of the damage variable  $D$  as a function of the applied displacement. Recall that fracture is predicted according to the proposed fracture model as  $D = 1$ . The comparison with the experiment shows that the displacement to fracture is underestimated in all three cases: by 20% for  $R = 6.67$  mm, by 27% for  $R = 10$  mm and by 32% for  $R = 20$  mm.

The underestimation of the displacement to fracture by the model is consistent with the aforementioned lower bound property of the proposed fracture envelope. However, the differences are large and require special attention. Firstly, we note that the relative error in the displacement to fracture depends on the specimen size. Due to the localization of plastic deformation, this error will become smaller, the longer the shoulders of the notched specimens. To shade more light on the discrepancies between the experimental results and the model predictions, we computed the evolution of the equivalent plastic strain and the stress triaxiality at the center of the notched specimens until the experimentally-measured displacement to fracture is reached (instead of stopping the computations at  $D = 1$ ). The corresponding plastic strain versus average stress triaxiality curves are shown as dashed red lines in Fig. 10. In this space, the discrepancies between the fracture envelope and the results from the notched tensile tests are even more pronounced. In the notched tensile tests, equivalent plastic strains as high as 0.35 are observed which is substantially higher than those measured at the surface in the butterfly specimens.

This observation is consistent with the lower bound property of the fracture envelope, but an enhanced model is needed in order to achieve a satisfactory prediction accuracy. Here, the following recommendations are made for future work:

- (1) Determine the strain to fracture based on FEA. All tested butterfly specimens featured the localization of plastic deformation within a narrow band. Both the stress triaxiality and the equivalent plastic strain inside the specimen may be very different from those at the specimen surface. Thus, it is proposed to determine the strain and stress state inside the specimen from detailed finite element simulations of each experiment. In addition to the local surface strain measurements, this approach requires the acquisition of global force and displacement histories.
- (2) Revisit the model formulation. There are numerous aspects of the simple empirical model given by Eq. (9) that need to be validated. The loading history in butterfly specimens is different from that in notched specimens. The first feature is a more or less constant stress triaxiality throughout loading, while stress triaxiality increases monotonically throughout the testing of the notched specimens. Thus, the assumption of a weighted damage accumulation may play an important role. Furthermore, it is worth recalling that the stress triaxiality and equivalent plastic strain are used to predict fracture for historic reasons: the first generation of void growth models made use of these two vari-

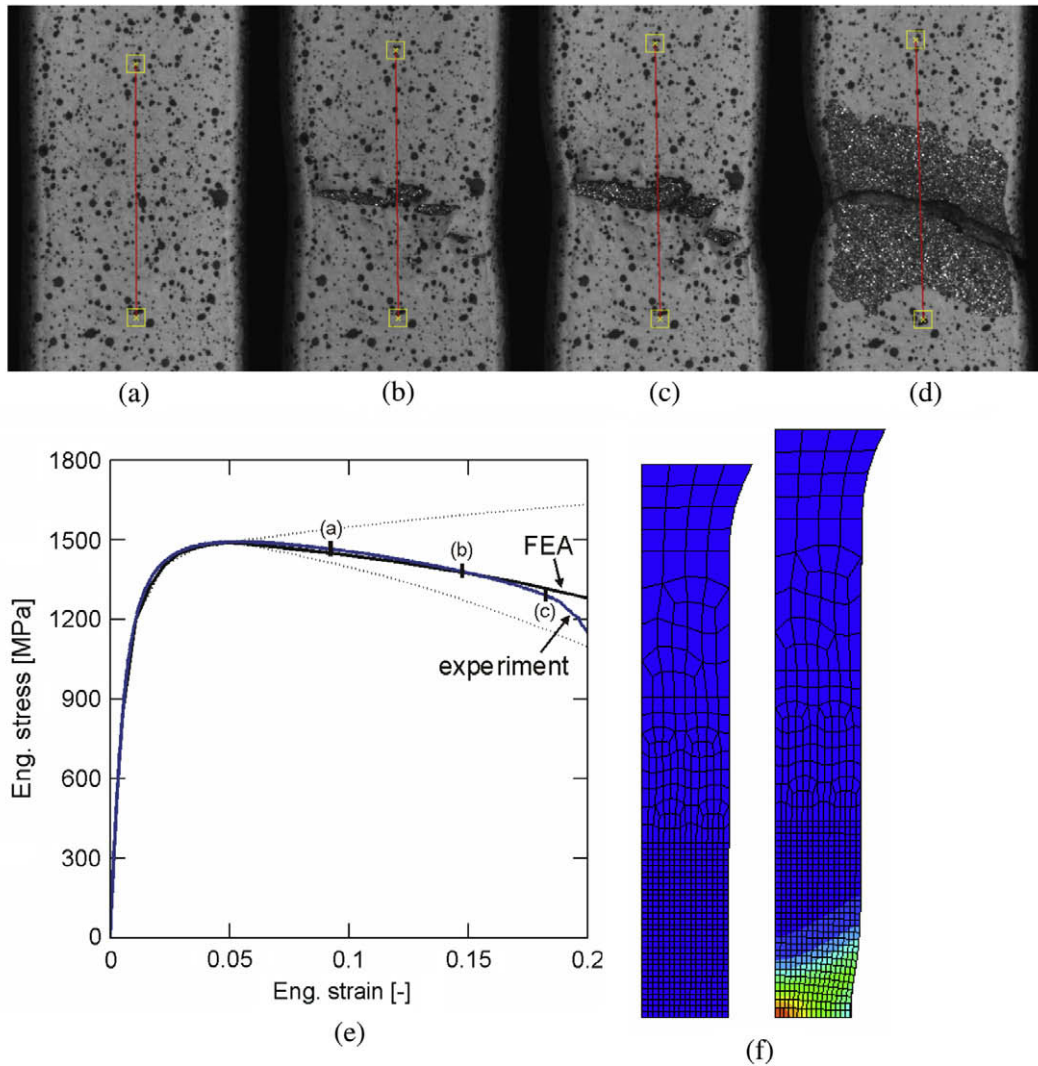


**Fig. 11.** (a)–(d) DIC photographs of the gage section at different stages of deformation. The red line shows the initially 6.5 mm long virtual extensometer; (e) blue curve shows the experimental engineering stress–strain curve; the solid black curves corresponds to the FEA prediction for a post-necking hardening modulus of  $H = 532$  MPa. The lower and upper dashed curves correspond, respectively, to  $H = 0$  and  $H = 3000$  MPa (linear extrapolation); (f) initial and deformed FEA mesh at an engineering strain of 0.19. The contour plot shows the equivalent plastic strain with a maximum of 0.55. (For interpretation of the references to color in this figure legend, the reader is referred to the web version of this paper.)

ables. However, more recent theoretical studies on porous materials indicate that the evolving morphological anisotropy because of pore shape changes and rotations may also play an important role. Thus, it may be needed to take additional variables into account to predict the onset of fracture.

#### 6.4. Fracture model calibration based on notched tensile tests

There are a couple of challenges which are specific to the martensitic sheet material. The plasticity tests indicated that the

machining of the specimens may have changed the material properties. It is also possible that the material properties near the center of a sheet (the butterfly specimens were only 0.4 mm thick) are different from those near the sheet surface (the notched specimens were 1.5 mm thick).

Based on the working assumption that the fracture properties of the 1.5 mm thick specimens are different from the 0.4 mm thick central layer that has been characterized by the butterfly experiments, we introduce a modified weighting function. The new empirical function  $g^*(\eta)$  is a piece-wise linear function for  $\eta \geq 0.33$  with only three support points:

- (1)  $\eta = 0.33$  – uniaxial tension,
- (2)  $\eta = 0.58$  – transverse plane strain tension,
- (3)  $\eta = 0.67$  – equi-biaxial tension.

**Table 2**  
Data points of the piece-wise linear approximation of the extrapolated true stress versus plastic strain curve  $\sigma(\varepsilon_p)$ .

$\varepsilon$	0	0.0014	0.004	0.0108	0.02	0.03	0.04	0.5
$\sigma$	750	1011	1214	1401	1494	1539	1569	1814

We have calibrated the values  $g^*(\eta)$  for  $\eta = 0.33$  and  $\eta = 0.58$  based on the notched and uniaxial tensile tests (error minimization for four tests through Monte-Carlo simulation). The corre-

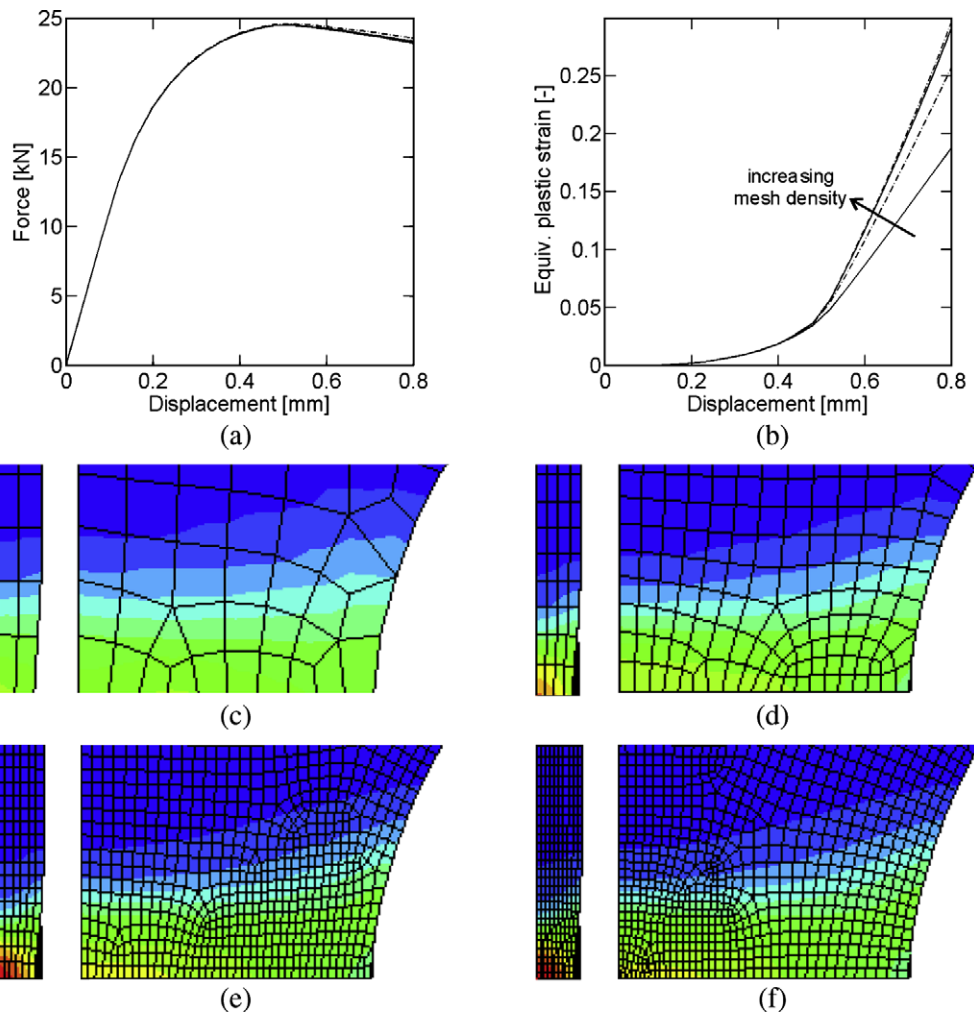


**Fig. 12.** Mesh size effect on simulation results for  $R = 6.67$  mm. (a) Force–displacement curves, (b) evolution of the equivalent plastic strain at the center of the specimen, (c)–(f) side and top view of the contour plots of the equivalent plastic strain for four different mesh densities near the specimen center. The maximum contour value (red color) is 0.3. (For interpretation of the references to color in this figure legend, the reader is referred to the web version of this paper.)

sponding data points are given in Table 3. Note that the previous value for equi-biaxial tension had been obtained from a punch test on the material of full-thickness and is hence included as support point.

All notched fracture simulations are repeated using  $g^*(\eta)$ . The results shown by dashed red curves in Fig. 13 indicate a good agreement with the experiments. Furthermore, the simulation of the uniaxial tensile test (with 6 solid elements through-the-thickness) predicts an engineering strain to fracture of 0.21 which is close to the experimental result of 0.20. Fig. 13 also shows the contour plot of  $D$  at the specimen mid-plane plane (left contour plots) and at the top surface. These plots reveal that the concentration of “damage” near the specimen center is most pronounced for a large notch radius (Fig. 13c).

## 7. Conclusions

Using two newly-developed experimental techniques, both the plasticity and fracture of martensitic steels have been studied under combined tensile and shear loading. The main conclusions drawn from this study are:

1. The planar isotropic Hill'48 yield surface along with an associated flow rule and isotropic hardening law provides accurate predictions of the stress–strain response over a wide range of multi-axial loading conditions.
2. In combination with the plasticity model, surface strain measurements have been used to quantify the stress triaxiality and the equivalent plastic strain history to fracture in butterfly-shaped specimens subject to multi-axial loading. Based on these measurements, a piece-wise linear curve has been determined in the equivalent plastic strain versus stress triaxiality plane to provide a lower bound of the fracture envelope.
3. This lower bound model has been used to predict the onset of fracture in notched tensile tests. The comparison of the numerical predictions with the experimental results shows a good agreement from an engineering point of view; however, the evaluation of the local strain and stress histories indicates that the lower bound model needs to be improved further. The analysis of the experiments has revealed that the local strains in the notched tensile tests are much higher than those admissible according to the lower bound model. An enhanced fracture envelope is proposed that predicts fracture during these tests with high accuracy.

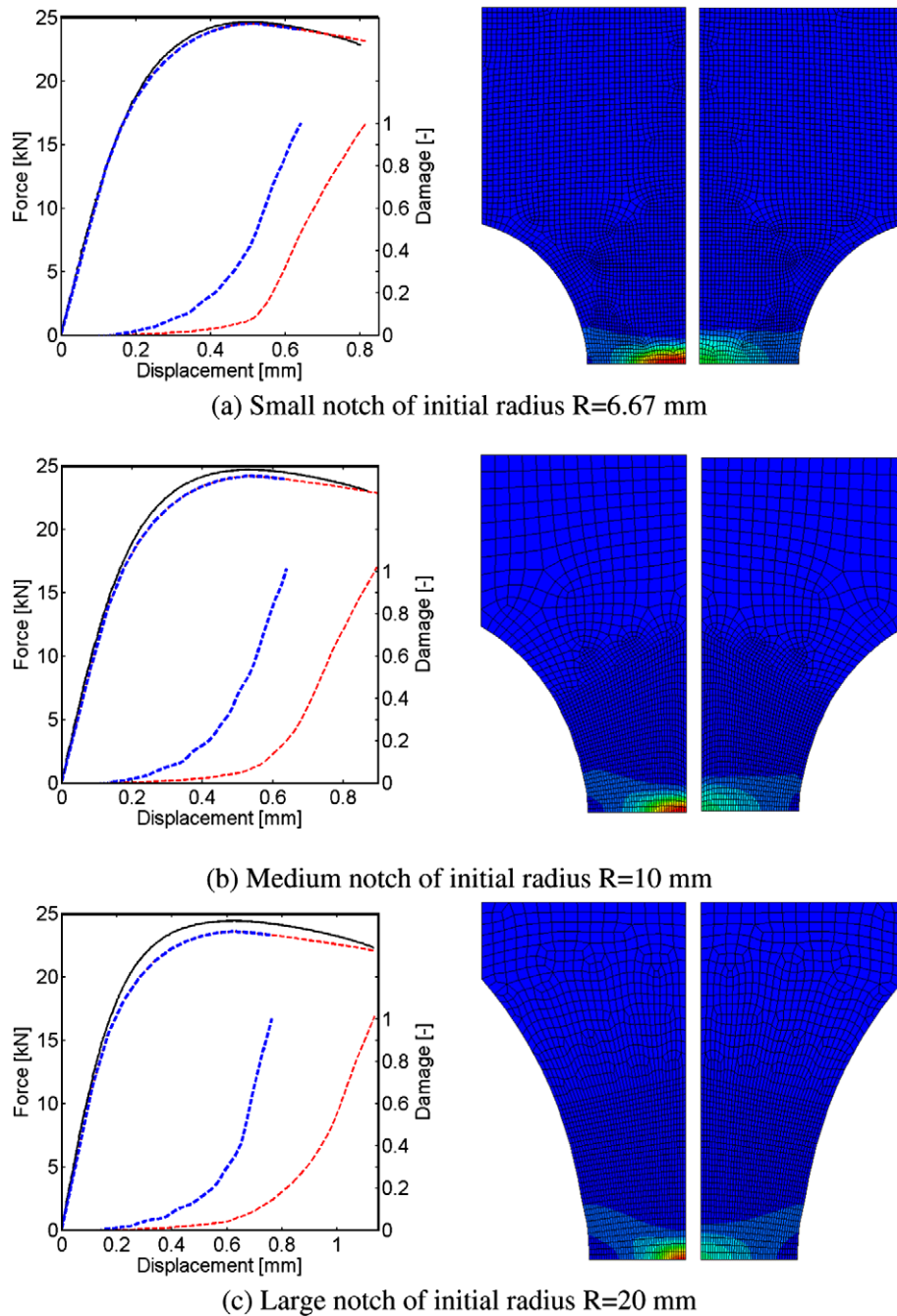


**Fig. 13.** The force–displacement curves are concave, while the convex-shaped curves show the damage accumulation; the black solid curves are experimental measurements; all simulation results are represented by dashed curves. The blue curves are obtained using the weighting function  $g$ , while the red curves correspond to the estimates based on  $g^*$ . The contour plots show the damage distribution at the onset of fracture (left: specimen mid-plane, right: top surface). The color spectrum in the contour plots increases from blue ( $D = 0$ ) to red ( $D = 1$ ). (For interpretation of the references to color in this figure legend, the reader is referred to the web version of this paper.)

**Table 3**  
Data points of the piece-wise linear fracture envelope  $g^*(\eta)$ .

$\eta$	0.33	0.58	0.67
$g^*$	1.5	0.19	0.39

### Acknowledgments

The partial support of the Joint MIT/Industry AHSS Fracture Consortium and the French National Center for Scientific Research (CNRS) is gratefully acknowledged. ThyssenKrupp Steel and Volkswagen are thanked for providing the material and specimens.

Thanks are also due to Professor T. Wierzbicki (MIT), Mr. Carey Walters (MIT) and Dr. L. Greve (VW) for valuable discussions. The authors are grateful to Altair Engineering for providing the HyperWorks software under academic license. Special thanks are due to the anonymous reviewers for their valuable comments that have led to major improvements of the manuscript.

### References

- Abaqus, 2007. Reference Manuals v6.7, Abaqus Inc.
- Bai, Y., 2008. Effect of loading history on necking and fracture, Ph.D. Thesis, Mechanical Engineering, Massachusetts Institute of Technology.

- Banu, M., Takamura, M., Hama, T., Naidim, O., Teodosiu, C., Makinouchi, A., 2006. Simulation of springback and wrinkling in stamping of a dual phase steel rail-shaped part. *J. Mater. Process. Technol.* 173, 178–184.
- Bao, Y., 2003. Prediction of ductile crack formation in uncracked bodies, Ph.D. Thesis, Ocean Engineering, Massachusetts Institute of Technology.
- Bao, Y., Wierzbicki, T., 2004. A comparative study on various ductile crack formation criteria. *J. Eng. Mater. Technol.* 126, pp-324.
- Barlal, F., Brem, J.C., Yoon, J.W., Chung, K., Dick, R.E., Choi, S.H., Pourboghrat, F., Chu, E., Lege, D.J., 2003. Plane stress yield function for aluminum alloy sheets. *Int. J. Plasticity* 19, 1297.
- Benzerger, A.A., Besson, J., Pineau, A., 2004. Anisotropic ductile fracture. Part II: theory. *Acta Mater.* 52, 4639–4650.
- Besson, J., Steglich, D., Brocks, W., 2003. Modeling of plane strain ductile rupture. *Int. J. Plasticity* 19, 1517–1541.
- Byun, T.S., Hashimoto, N., Farrell, K., 2004. Temperature dependence of strain hardening and plastic instability behaviors in austenitic stainless steels. *Acta Mater.* 52, 3889–3899.
- Chen, P., Koc, M., 2007. Simulation of springback variation in forming of advanced high strength steels. *J. Mater. Process. Technol.* 190, 189–198.
- Chien, W.Y., Pan, J., Tang, S.C., 2001. Modified anisotropic Gurson yield criterion for porous ductile sheet metals. *J. Eng. Mater. Technol.* 123, 409.
- Clift, S.E., Hartley, P., Sturgess, C.E.N., Rowe, G.W., 1990. Fracture prediction in plastic deformation processes. *Int. J. Mech. Sci.* 32, 1–17.
- Cockcroft, M.G., Latham, D.J., 1968. Ductility and the workability of metals. *J. Inst. Met.* 96, 33–39.
- Danas, K., Ponte Castaneda, P., 2009. A finite-strain model for anisotropic viscoplastic porous media: II-Applications. *Eur. J. Mech.* A 28, 402–416.
- Durrenberger, L., Molinari, A., Rusinek, A., 2008. Internal variable modeling of the high strain-rate behavior of metals with applications to multiphase steels. *Mater. Sci. Eng. A* 478, 297–304.
- Gurson, A.L., 1977. Continuum theory of ductile rupture by void nucleation and growth. Part I: yield criteria and flow rules for porous ductile media. *J. Eng. Mater. Technol.* 99, 2–15.
- Hershey, A.V., 1954. Plasticity of isotropic aggregate of anisotropic facecentered cubic crystals. *J. Appl. Mech.* 21, 241–249.
- Hill, R., 1948. A theory of the yielding and plastic flow of anisotropic metals. *Proc. Roy. Soc. Lond. A* 193, 281–297.
- Lassance, D., Fabregue, D., Delannay, F., Pardoën, T., 2007. Micromechanics of room and high temperature fracture in 6xxx Al alloys. *Prog. Mater. Sci.* 52, 62–129.
- Leblond, J.B., Mottet, G., 2008. A theoretical approach of strain localization within thin planar bands in porous ductile materials. *C. R. Mecanique* 336, 176–189.
- Leblond, J.B., Perrin, G., Devaux, J., 1995. An improved Gurson-type model for hardenable ductile metals. *Eur. J. Mech. A* 14 (2), 499–527.
- Lee, M.-G., Kim, D., Kim, C., Wenner, M.L., Wagoner, R.H., Chung, K., 2005. Springback evaluation of automotive sheets based on isotropic-kinematic hardening laws and non-quadratic anisotropic yield functions. Part II: characterization of material properties. *Int. J. Plasticity* 21, 883–914.
- LeRoy, G., Embury, J.D., Edward, G., Ashby, M.F., 1981. A model of ductile fracture based on the nucleation and growth of voids. *Acta Metall.* 29, 1509–1522.
- McClintock, F.A., 1968. A criterion of ductile fracture by the growth of holes. *J. Appl. Mech.* 35, 363–371.
- Mohr, D., Dunand, M., 2008. Optimized specimen for the fracture testing of advanced high strength steels under combined normal and shear loading. Technical Report 182, Impact and Crashworthiness Laboratory, Massachusetts Institute of Technology.
- Mohr, D., Henn, S., 2004. A New method for calibrating phenomenological crack formation criteria, Technical Report 113, Impact and Crashworthiness Laboratory, Massachusetts Institute of Technology.
- Mohr, D., Henn, S., 2007. Calibration of stress-triaxiality dependent crack formation criteria: a new hybrid experimental–numerical method. *Exp. Mech.* 47 (6), 805–820.
- Mohr, D., Oswald, M., 2008. A new experimental technique for the multi-axial testing of advanced high strength steel sheets. *Exp. Mech.* 48 (1), 65–77.
- Naderi, M., Saeed-Akbari, A., Bleck, W., 2008. The effects of non-isothermal deformation on martensitic transformation in 22MnB5 steel. *Mater. Sci. Eng. A* 487, 445–455.
- Nahshon, K., Hutchinson, J.W., 2008. Modification of the Gurson model for shear fracture. *Eur. J. Mech. A* 27, 1–17.
- Norris, D.M., Moran, B., Scudder, J.K., Quinones, D.F., 1978. A computer simulation of the tension test. *J. Mech. Phys. Solids* 26, 1–19.
- Oh, S., Chen, C.C., Kobayashi, S., 1979. Ductile failure in axisymmetric extrusion and drawing. Part 2. Workability in extrusion and drawing. *J. Eng. Ind.* 101, 36–44.
- Padmanabhan, R., Baptista, A.J., Oliveira, M.C., Menezes, L.F., 2007. Effect of anisotropy on the deep-drawing of mild steel and dual-phase steel tailor-welded blanks. *J. Mater. Process. Technol.* 184 (1–3), 288–293.
- Pardoën, T., 2006. Numerical simulation of low stress triaxiality ductile fracture. *Comput. Struct.* 84, 1641–1650.
- Pardoën, T., Delannay, F., 1998. Assessment of void growth models from porosity measurements in cold drawn copper bars. *Metall. Mater. Trans. A* 29, 1895–1909.
- Pardoën, T., Hutchinson, J.W., 2000. An extended model for void growth and coalescence. *J. Mech. Phys. Solids* 48 (12), 2467–2512.
- Rice, J.R., Tracey, D.M., 1969. On the ductile enlargement of voids in triaxial stress fields. *J. Mech. Phys. Solids* 17, 201–217.
- Steglich, D., Brocks, W., Heerens, J., Pardoën, T., 2008. Anisotropic ductile fracture of Al2024 alloys. *Eng. Fract. Mech.* 75, 3692–3706.
- Tarigopula, V., Hopperstad, O.S., Langseth, M., Clausen, A.H., 2008. Elastic–plastic behaviour of dual-phase, high-strength steel under strain-path changes. *Eur. J. Mech. A* 27, 764–782.
- Tvergaard, V., 2008. Shear deformation of voids with contact modeled by internal pressure. *Int. J. Mech. Sci.* 50, 1459–1465.
- Tvergaard, V., Needleman, A., 1984. Analysis of the cup-cone fracture in a round tensile bar. *Acta Metall.* 32, 157–169.
- Voyiadjis, G.Z., Kattan, P.I., 1992. A plasticity-damage theory for large deformation of solids. Part 1. Theoretical formulation. *Int. J. Eng. Sci.* 30 (9), 1089–1108.
- Wierzbicki, T., Xue, L., 2005. On the effect of the third invariant of the stress deviator on ductile fracture. Technical Report 136, Impact and Crashworthiness Laboratory, Massachusetts Institute of Technology.
- Wierzbicki, T., Bao, Y., Bai, Y., 2005. A new experimental technique for constructing a fracture envelope of metals under multi-axial loading. In: Proceedings of the 2005 SEM Annual Conference and Exposition on Experimental and Applied Mechanics, pp. 1295–1303.
- Yoshida, F., Uemori, T., Fujiwara, K., 2002. Elastic–plastic behavior of steel sheets under in-plane cyclic tension–compression at large strain. *Int. J. Plasticity* 18, 633–659.